Chinese Journal of Aeronautics, (2014),27(4): 772–780

Chinese Society of Aeronautics and Astronautics
& Beihang University

Chinese Journal of Aeronautics

cja@buaa.edu.cn
www.sciencedirect.com

Low-frequency unsteadiness of vortex wakes over slender bodies at high angle of attack

Ma Baofeng *, **Huang Yu, Liu Tongxin**

Ministry-of-Education Key Laboratory of Fluid Mechanics, Beihang University, Beijing 100191, China

Received 5 August 2013; revised 18 March 2014; accepted 25 March 2014
Available online 4 July 2014

KEYWORDS

Aerodynamics;
Experiments;
Fluid dynamics;
Unsteady flow;
Vortex flow

Abstract A type of flow unsteadiness with low frequencies and large amplitude was investigated experimentally for vortex wakes around an ogive-tangent cylinder. The experiments were carried out at angles of attack of 60–80° and subcritical Reynolds numbers of $0.6–1.8 \times 10^5$. The reduced frequencies of the unsteadiness are between 0.038 and 0.072, much less than the frequency of Karman vortex shedding. The unsteady flow induces large fluctuations of sectional side forces. The results of pressure measurements and particle image velocimetry indicate that the flow unsteadiness comes from periodic oscillation of the vortex wakes over the slender body. The time-averaged vortex patterns over the slender body are asymmetric, whose orientation is dependent on azimuthal locations of tip perturbations. Therefore, the vortex oscillation is a type of unsteady oscillation around a time-averaged asymmetric vortex structure.

1. Introduction

It has long been known that axisymmetric slender bodies can produce asymmetric vortex wakes at high angles of attack (AOAs), even with zero sideslip.[1–9] The asymmetric vortices can induce large time-averaged side forces which are sometimes even beyond normal forces. Previous research has revealed that the vortex asymmetry primarily arising from imperfections on the nose-tip of a body[3–5] and even natural perturbation from machining tolerance can trigger the development of the asymmetric vortex flow. Since the distribution of machining tolerance is different and random in various models, the experimental results normally show poor reproducibility. If an artificial perturbation, however, is added onto the nose-tip, it can suppress the natural perturbation and dominate the development of the asymmetric vortex flow. By doing this, reproducible time-averaged results can be obtained because the artificial perturbation, its size and position, are pre-determined.[5] The sensitivity of vortex flows over slender bodies to tip imperfections has been exploited for vortex control.[8–10]

The previous experiments[1,6] have revealed that asymmetric vortex wakes over a slender body exhibit a time-averaged multi-vortex structure with an alternate arrangement along a body axis at high AOAs. In the asymmetric vortex system, when a higher vortex breaks away from the body, a new vortex will be yielded under it. As a result, an alternate multi-vortex pattern is formed. However, the flow pattern at the after-body part far away from the fore-body will transit to Karman vortex

* Corresponding author. Tel.: +86 10 82338344.
E-mail address: bf-ma@buaa.edu.cn (B. Ma).

Peer review under responsibility of Editorial Committee of CJA.

Production and hosting by Elsevier

http://dx.doi.org/10.1016/j.cja.2014.06.011

shedding at some locations downstream if the cylinder part is sufficiently long.[6,11–13]

Besides the vortex shedding at an after-body, some intrinsic unsteady features also exist for the vortex system, as summarized in the review paper.[14] The unsteady characteristics of asymmetric vortices were examined in detail by Degani et al.[15–17] They found initially unsteadiness on flow fields over slender bodies using numerical simulation,[15] thus carrying out experiments to identify these unsteady flows.[16] Their experiments revealed three types of unsteady phenomena, including low-frequency Karman vortex shedding, high-frequency shear-layer unsteadiness, and vortex interaction at moderate frequencies. Among these unsteady phenomena, low-frequency vortex shedding has the largest fluctuating amplitude, but can be suppressed by a splitter plate on the leeward side of the body.[17] However, in Degani et al.'s experiments, the pressure transducers for monitoring pressure signals were distributed only on the cylinder part of the slender body, so the unsteadiness for fore-body vortices could not be detected. It is expected that with increasing AOAs, the higher vortex will break away from the body surface earlier and the whole vortex system will move forward in position. Therefore, at sufficiently high AOAs, the time-averaged asymmetric vortices will be retained only at the fore-body part. The experiments by Zilliac et al.[18] using a smoke visualization showed qualitatively that at AOAs of more than 65°, the flow could be divided into three parts: a pair of stationary vortices over a fore-body, oblique shedding over a cylinder part adjacent to the fore-body, and parallel shedding around an inclined cylinder part far downstream. They believed that the vortices near the fore-body were nearly stationary with no significant unsteadiness. Hoang et al.[19] measured the unsteady flow fields around a hemisphere-cylinder body using hotwires and detected a type of unsteady phenomenon where the frequencies of fluctuations are lower than the ones of Karman vortex shedding, but the sources of fluctuations were not clear, and they conjectured that the low frequency fluctuations could be caused by fore-body vortex heaving. Ma et al.[20,21] also studied the difference of unsteadiness at the fore-body and after-body of a slender body at extreme high AOAs. The pressure signals' measured and associated spectra indicated that the unsteadiness was primarily Karman vortex shedding at the after-body, but there exists lower frequency fluctuations at the fore-body. They speculated that the lower-frequency fluctuations come from fore-body vortex fluctuations.

The previous studies mentioned above implied that a type of low-frequency unsteady phenomena seemed to exist around the fore-body of a slender body at high AOAs, frequencies of which are lower than the ones of Karman vortex shedding. However, the previous studies only presented the results based on single-point measurements, so the effects of the unsteady phenomena on the side forces of slender bodies cannot be evaluated. More importantly, the flow sources of these fluctuations need to be confirmed further. In addition, the variation of the unsteady fluctuations with Reynolds numbers is also an interesting issue worth research.

The present study will focus on the vortex unsteadiness around the fore-body of a slender body at sufficiently high AOAs and try to answer the above questions based on multi-points pressure and particle image velocimetry (PIV) measurements.

2. Experimental setup

All experiments were carried out in the D4 Wind Tunnel of Institute of Fluid Mechanics of Beihang University (BUAA). The wind tunnel is a low speed, low noise and closed-return tunnel that can be run with either an open or closed test section. The test sections are 1.5 m wide, 1.5 m high and 2.5 m long, with a turbulence level of less than 0.1%. The open test section was used in the present experiments, and the model layout in the wind tunnel is illustrated in Fig. 1(a). The AOAs of the model are varied through sideslip angles for performing PIV more conveniently. The laser sheet for PIV illuminates the leeward side of the fore-body normal to the body's axis from one side. The PIV snapshots were taken from a front view, but presented in their mirror images in the following "Results" section, equivalently seen from a rear view.

The experimental model is a pointed ogive-tangent cylinder with a fineness ratio of 8D, including a 3D fore-body (D is the diameter of cylinder, and D = 90 mm), as shown in Fig. 1(b). There is a small rotatable nose of 27.5 mm at the front of the fore-body, which is used to change the orientation of tip perturbations. An artificial tip perturbation was added on the nosetip in order to suppress natural imperfections on the tip, ensuring the repeatability of time-averaged flow fields, as shown in Fig. 1(b) (d is the diameter of tip perturbation, d = 0.2 mm). The perturbation is placed on two azimuthal angles of +45° and −45° in experiments.

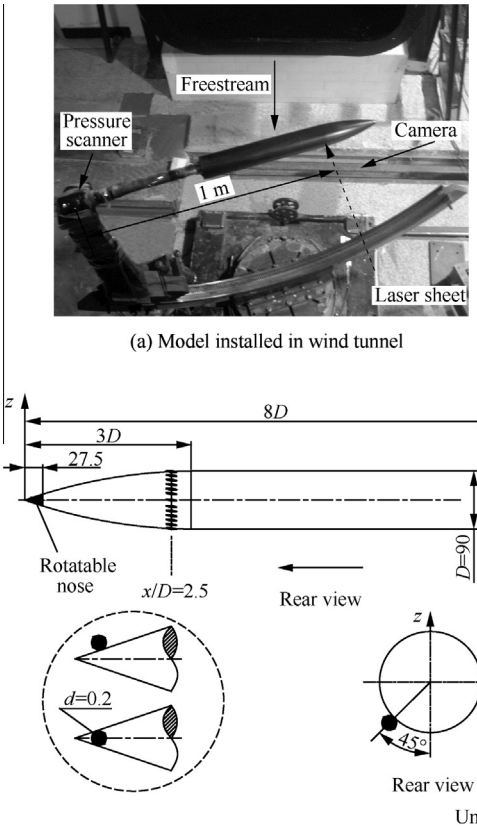

Fig. 1 Experimental layout and model.

The present investigation chiefly focuses on the flow around the fore-body, so a ring of pressure taps was distributed uniformly at the section of $x/D = 2.5$ with totally twenty-four measurement points. Sectional side forces was calculated by the integration of surface pressures. The pressure taps were connected with micro pressure scanners through soft tubes. The pressure scanner used is the ESP-64HD scanner of Pressure System Inc. with 64 channels and the associated acquisition system is the DTC Initium. The sampling rate of the system is 330 Hz and the time interval between channels is 50 μs. For unsteady pressure measurements, the tubing should have proper length to satisfy the requirements for pressure signal responses. Therefore, in order to estimate the effect of tubes on unsteady pressure measurements, a measurement system for dynamic responses of pressure tubes was established to gain the frequency characteristics of the tubes with various lengths, as shown in Fig. 2(a). In this system, a loudspeaker driven by an electrical signal generator was used to produce sinusoid pressure signals with a variety of frequencies f as input signals measured. The input signals are divided into two outputs, one of which is directly connected with one channel in the pressure scanner and the other is connected with one of other channels through a measured tube. The response characteristics can obtained by comparing the difference between the pressure signals sampled from the two channels. Because all of the pressure tubes used in the present experiments is 1 m long, the frequency characteristics of the pressure tube with a length of 1 m are shown in Fig. 2(b). It can be seen that

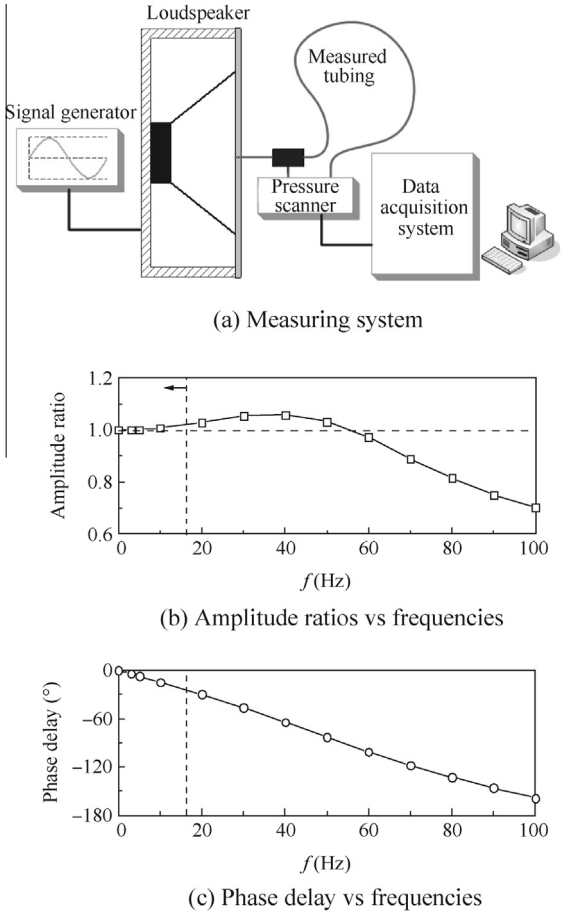

Fig. 2 Frequency characteristics of pressure tube with 1 m.

the amplitudes of the pressure signals acquired will be 2.8% higher than the real values when input pressure signals are 20 Hz. In the present experiments, the pressure fluctuation frequencies are not more than 16 Hz, so the pressure tube used will lead to the amplitude error of less than 2.8%. The phase delay is shown in Fig. 2(c), which is not large and also not important in the context of the present investigation. Therefore, the present scheme was capable of satisfying the requirement for dynamic pressure measurements. In addition, the sampling rate (330 Hz) of pressure measurements were sufficiently high to avoid signal aliasing, because the pressure tubing is analogous to a low-pass filter for pressure responses, and can filter out possible higher frequency signals than the ones being able to be measured, eliminating their effects on lower frequencies signals required.

The spatial vortex structures over the slender body are obtained using Dantec PIV. In the PIV measurement, the airflow was seeded with micro-sized oil particles generated by an atomizer and vegetable oil, and the oil particles are illuminated by a sheet of laser light. Images were acquired with a Hisense 4 M digital camera (2048×2048 pixels). Image pairs were correlated with a two-step windowing process incorporating window shifting to determine particle displacements. Typical velocity fields comprised 85×85 velocity vectors, using a window overlap of 25%. It should be noted that the PIV system is not time-resolved for the present measurements. The maximal sampling rate of the PIV is 3.15 Hz due to the performance limitation of the laser and camera, while the lowest frequency for the unsteady fluctuations to be measured in experiments is 6.6 Hz at a wind speed of 10 m/s, so the PIV measurement is unable to satisfy the Nyquist sampling theorem. Therefore, the PIV measurements were just used to qualitatively demonstrate the unsteady behavior of asymmetric vortices, unable to record complete evolution of flow patterns. In spite of this limitation, it is believed that adequate information on instantaneous flow structures can be obtained if the number of PIV snapshots is large enough.

The freestream speeds in experiments are at a range of 10–40 m/s, and the corresponding Reynolds numbers based on the cylinder diameter D are from 0.6×10^5 to 2.5×10^5. The AOAs are from 0° to 90°, but the emphasis is put in the range of 60–80°. The repeatability for the pressure and PIV measurements has been examined, and the specific precision for the measurements will be given with the results together in the following text.

3. Results

In this section, the instantaneous sectional side forces from pressure integration are represented in a time domain and a frequency domain. The time-dependent pressure distributions and PIV snapshots are also given for exploring unsteady flow patterns causing fluctuations.

3.1. Sectional side forces

Fig. 3 shows the time-averaged value C_{ym} (C_{ym} is a time-averaged sectional side force coefficient) and root mean square (RMS) of sectional side forces from 0° to 90° AOAs, which were obtained by averaging 2000 sampling points, and the artificial tip perturbation is located at two azimuthal locations of

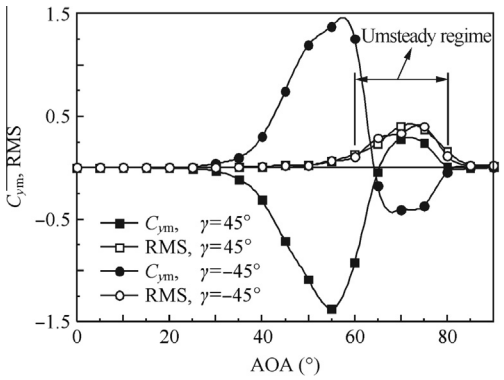

Fig. 3 C_{ym} and RMS vs AOA.

+45° and −45°. In the figure, wind speed $U = 10$ m/s, Reynolds number $Re = 0.6 \times 10^5$, $x/D = 2.5$, and γ is azimuthal angle of tip perturbation around a body axis. It can be seen that the time-averaged side forces start to rise at 30° AOA due to fore-body vortices symmetry breaking and attain the maximum at 55° AOA, then decrease. The side forces change the direction at AOAs of 65–80°, which is caused by the forward movement of the asymmetric vortex system with increasing AOAs. At this range of AOAs, the $x/D = 2.5$ section has been located at a three-vortex regime from a two-vortex regime due to the multi-vortex structure of the vortex wakes.[1,6] Beyond 80° AOA, a concentrated vortex system is unable to be formed over the fore-body, so the time-averaged side forces become zero. For the two azimuthal locations of the artificial tip perturbation, the associated side forces are almost mirror-imaged, which stem from bi-stable switching of asymmetric vortices. The present results of time-averaged side forces are comparable to the previous research.[5,6,22]

Besides the time-averaged results, Fig. 3 also presents the RMS of instantaneous side forces for two locations of the tip perturbation, and the fluctuation magnitudes for the two cases are similar. The RMS of side forces between the angles-of-attack of 65° and 80° is apparently higher than the ones at other AOAs, which is the unsteady regime to be focused on in the investigation. Corresponding to the unsteady regime, the time histories of instantaneous sectional side force coefficients C_y at various AOAs are illustrated in Fig. 4. In the figure, α is the angle of attack, $\gamma = 45°$, $U = 20$ m/s, $Re = 1.2 \times 10^5$, and $x/D = 2.5$. Since the time-averaged side forces are different at various AOAs, the upper limit and the lower limit for each graph in Fig. 4 are set to be different in order to display each time history in the central part of a graph. However, the differences between the upper and lower limits are all the same, so the fluctuation amplitudes between time histories can be intuitively compared without any deformation. At the AOAs of 55° and 60°, the time-averaged side forces are higher, but the unsteady fluctuations are not much apparent and the amplitudes are lower. Larger amplitude fluctuations begin with the AOA of 65° and end up with the AOA of 80°, and it can also be seen qualitatively that the frequencies will grow with increasing AOAs. At the AOA of 85°, both the time-averaged value and instantaneous values of side forces almost reduce to zero.

The effects of Reynolds numbers on unsteady fluctuations at a fixed AOA are depicted in Fig. 5. In the figure, $\gamma = 45°$, $\alpha = 70°$, and $x/D = 2.5$. At the Reynolds numbers of

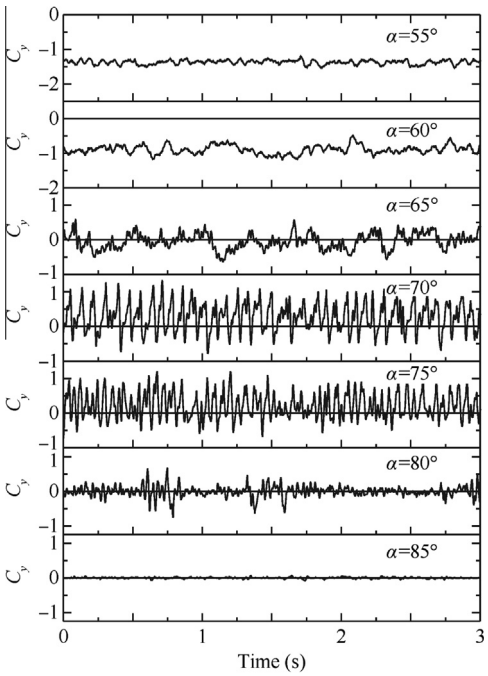

Fig. 4 Time histories of sectional side force coefficients at various AOAs.

0.6×10^5–1.8×10^5, the time histories of side forces all exhibit large amplitude fluctuations and the absolute frequencies increase with increasing Reynolds numbers. With the Reynolds number greater than 2.1×10^5, the fluctuation amplitudes abruptly decrease. Through analyzing pressure distributions in the following text, it will be found that boundary

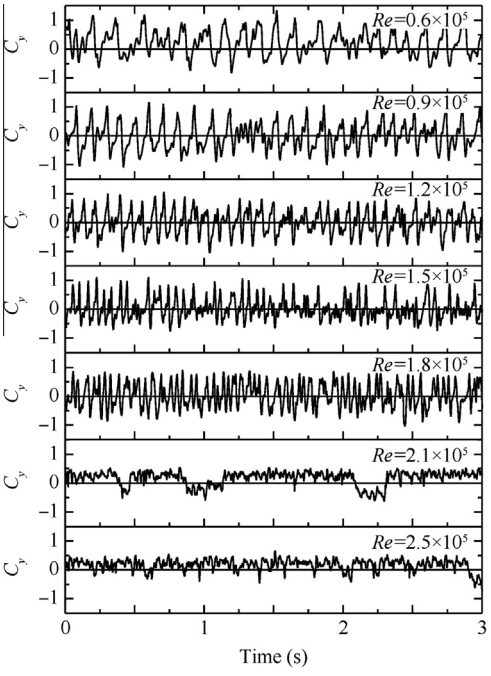

Fig. 5 Time histories of sectional side forces at various Reynolds numbers.

layers undergo transition from laminar separation to turbulent separation at the Reynolds number of 2.1×10^5, and this variation of flow separation types can modify asymmetric vortex patterns.

Fig. 6 presents the frequency spectra for time histories of side forces in Fig. 5, which can reveal quantitatively the frequency variation with Reynolds numbers. The spectra were obtained using fast Fourier transformation (FFT) on time histories of side forces. The mean values of side forces were subtracted from the associated time histories before FFT in order to more clearly display frequency peaks, and a Hamming window is also added for reducing "frequency leakage". The frequency spectra show that the non-dimensional reduced frequencies of the fluctuation are at a range of 0.038–0.072 for current Reynolds numbers and AOAs, and the reduced frequencies are also much less than the frequency of Karman vortex shedding of 0.21. It should be noted that the pressure tubing for pressure measurements is similar to a low-pass filter and can filter out high frequency fluctuation components. For the present layout of tubing, however, the pressure signals of less than 60 Hz are not attenuate, as shown in Fig. 2. Therefore, if there is Karman vortex shedding in flow fields, it will be able to be detected through pressure measurements. The reduced frequencies roughly decrease with increasing Reynolds number as illustrated in Fig. 6(a)–(e). It can also be found that the frequencies are higher at higher AOAs, as shown in Fig. 6(a) and (f). In addition, the isolated frequency peaks are very clear and clean at lower Reynolds numbers in Fig. 6(a) and (f), and at higher Reynolds numbers the frequency spectra include additional frequency components. However, only the dominant frequencies are considered in the present analysis.

The measurement precision for the time-averaged values C_{ym}, RMS and reduced frequencies f^* of instantaneous side forces is shown in Table 1 at $Re = 0.6 \times 10^5$ and 1.2×10^5 with $\alpha = 70°$ and 75°. The standard deviations σ of the above

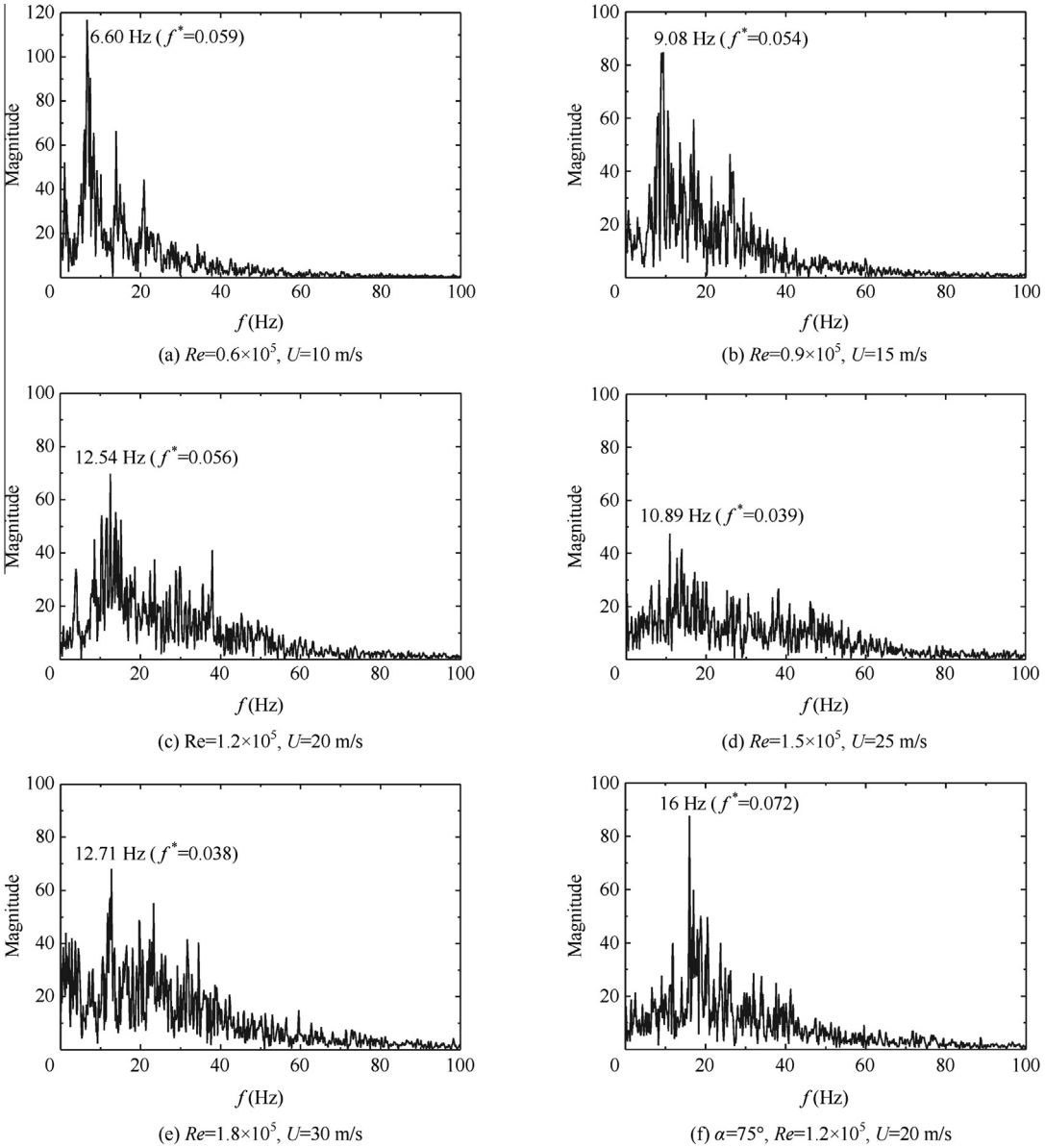

Fig. 6 Frequency spectrum of sectional side forces at various Reynolds numbers ($\alpha = 70°$ and $f^* = fD/U$).

Table 1 Measurement precision of C_{ym}, RMS and f^*.

Condition	C_{ym}	RMS	f^*
$\alpha = 70°$, $Re = 0.6\times10^5$	0.012	0.012	0.0022
$\alpha = 70°$, $Re = 1.2\times10^5$	0.013	0.011	0.0033
$\alpha = 75°$, $Re = 0.6\times10^5$	0.010	0.016	0.0024
$\alpha = 75°$, $Re = 1.2\times10^5$	0.011	0.006	0.0047

quantities was calculated based on seven repeatability measurements, and it can be seen that the measurement precision is good.

3.2. Pressure distributions and PIV results

In order to reveal the flow mechanism resulting in the side-force fluctuations, instantaneous pressure distributions and PIV snapshots at $x/D = 2.5$ over the slender body are given in this subsection. One of the advantages for the present measuring system based on tubing and pressure scanners is that more pressure taps can be distributed on the model, thus being capable to measure the evolution of unsteady pressure distributions. Unlike a hotwire or flush-mounted dynamic pressure transducers, only very few discrete measurement points can be obtained. The sectional pressure distributions are very helpful to explore the characteristics of the asymmetric vortex flow. Fig. 7(a) shows the transient evolution of sectional pressure distributions nearly at one fluctuation period. In the figure, θ is the azimuthal angle of pressure taps around a body, C_p is the pressure coefficient. The real sampling interval is 3.03 ms, but the data are re-sampled with an interval of 6.06 ms to display profiles more clearly. The asymmetric pressure distributions in Fig. 7(a) exhibit typical laminar separation on both sides of the body, and the separation angles are about $\pm 90°$. The method of identifying separation types in terms of pressure distributions is based on previous research.[22,23] The pressure suction peaks are induced by the lower vortex in an asymmetric vortex pair adjacent to the body surface. At $\alpha = 70°$, the third vortex in a multi-vortex structure of a slender body has moved forward beyond the $x/D = 2.5$ section, so the pressure distribution there has been dominated by the lower vortex of the nose vortex pair and the third vortex under the original higher vortex. The following PIV results will show this vortex pattern more clearly. In Fig. 7(a), the variation of vortex suction peaks strongly implies that the asymmetric vortices over the fore-body vary with time. However, since the suction peaks always locate at the right side in a period, the movements of fore-body vortices are more likely to oscillate around a time-averaged asymmetric structure instead of shedding alternately.

Furthermore, the pressure fluctuations primarily come from the leeward side, particularly under vortices, whereas they are much weaker on the upwind side, as depicted in Fig. 7(a). The time histories of pressure signals at both sides of the leeward side are shown in Fig. 7(b) and (c). The fluctuation is relatively weak on the left side (Fig. 7(b)), whereas the amplitudes are very high on the right side due to locating near the suction peak (Fig. 7(c)). Though the fluctuation levels are different for two pressure signals, they are highly correlated with each other.

The correlation relationship is quantitatively illustrated in Fig. 8 where the individual frequency spectrum and correlation spectrum for two pressure signals are calculated. Two pressure

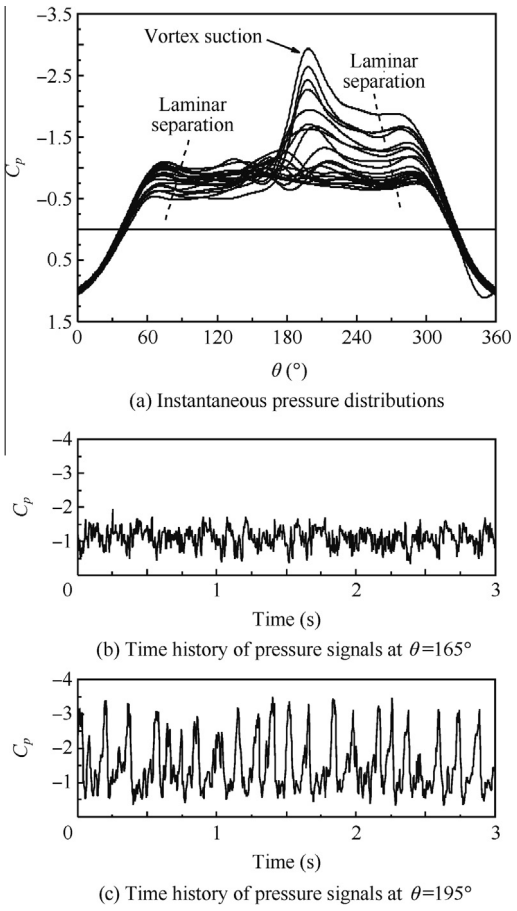

Fig. 7 Instantaneous pressures ($U = 10$ m/s, $Re = 0.6\times10^5$, $\alpha = 70°$).

signals have the same frequency (Fig. 8(a) and (b)), and their phase difference is approximately 180° (175.6°). The phase difference can also be found qualitatively at time history curves (Fig. 7(b) and (c)) if the graphs are amplified, where a wave crest in one time history corresponds to a wave trough in another one. The reverse phase fluctuation on both sides of the leeward side implies that the vortex movement is alternate oscillation by two vortices, not in-phase oscillation of two vortices or one-vortex oscillation.

With increasing Reynolds numbers, boundary layers on a slender body can yield turbulent separation. As a result, the vortex fluctuation will be weakened significantly, as mentioned above in Fig. 5, and Fig. 9(a) further shows the time-averaged pressure distributions from lower to higher Reynolds numbers. In the figure, and SP denotes separation point. When $Re < 1.8\times10^5$, boundary layers are all laminar separation on both sides of body, and the separation points are roughly $\pm 90°$. At $Re = 1.8\times10^5$, they are laminar separation on the left side with a separation point of 90°, but turbulent separation on the right with a separation point of $-150°$. When $Re > 1.8\times10^5$, they all change to turbulent separation on both sides with the separation points of $\pm 120°$. Fig. 9(b) shows the instantaneous pressure distributions where the boundary layers all apparently exhibit typical turbulent separation on both sides of the body at any instant. The vortex suction originally existing at lower Reynolds numbers disappears, and the levels of pressure fluctuations are also reduced greatly.

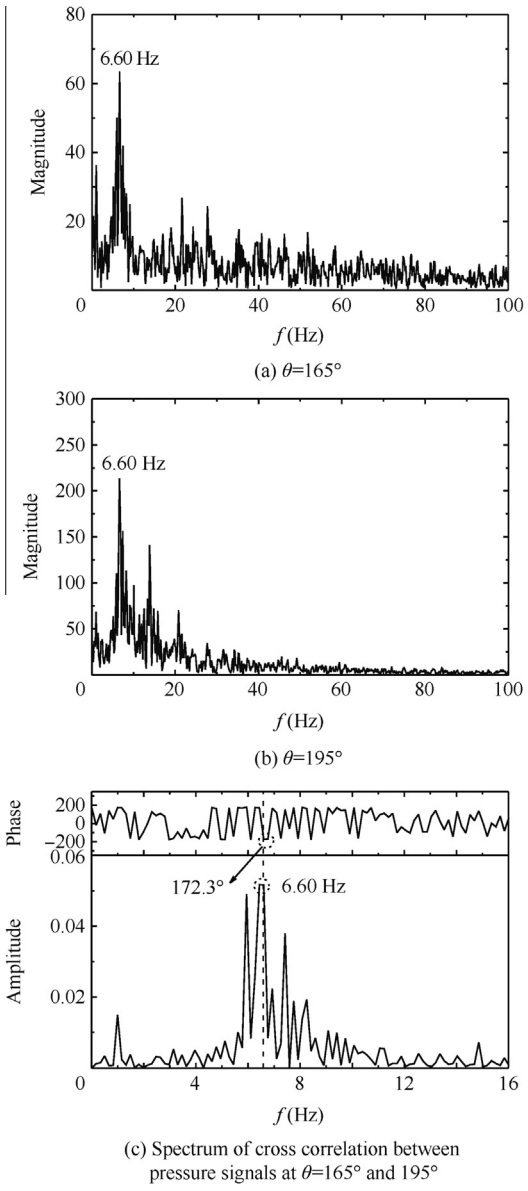

Fig. 8 Frequency spectrum of pressure signals ($U = 10$ m/s, $Re = 0.6 \times 10^5$, $\alpha = 70°$).

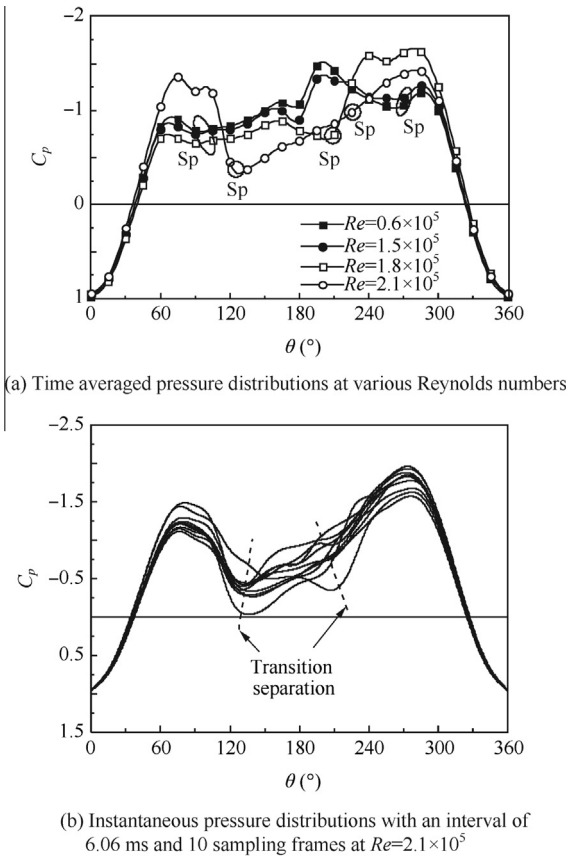

Fig. 9 Pressure distributions ($\alpha = 70°$, $U = 35$ m/s).

Table 2 Measurement precision of C_{pm}, RMS, and f^* at $\alpha = 70°$ and $Re = 0.6 \times 10^5$.

θ (°)	C_{pm}	RMS	f^*
165	0.017	0.006	0.0028
195	0.017	0.011	0.0023

Corresponding to Table 1 and 2 shows the time-averaged values C_{pm}, RMS, and reduced frequencies f^* of instantaneous pressures in Fig. 8(b) and (c), and the standard deviations are also calculated based on seven repeatability measurements. The pressures and side forces have almost the same magnitude of precision, because the side forces come from pressure integration.

Figs. 10 and 11 present the asymmetric vortex patterns at $x/D = 2.5$ over the slender body based on PIV measurements. In the figure, σ is RMS of absolute velocity fields ($\sqrt{u^2 + v^2}$). The time-averaged flow structures with $\gamma = \pm 45°$ are shown in Fig. 11(a) and (b), and two asymmetric vortex patterns are mirror-imaged. The fluctuations of pressures and side forces are mainly dominated by the two vortices closer to body surface. At $\alpha = 70°$, the flow pattern is a three-vortex structure at $x/D = 2.5$, so there should exist one higher vortex above the lower vortex which is also the highest vortex in the three-vortex structure. However, since the highest vortex is unsteady and moves up and down with large amplitudes in a normal direction, it can be found only in an instantaneous result (see Fig. 11), whereas being smoothed out at time-averaged PIV results in Fig. 10(a) and (b). Besides the time-averaged results, the PIV measurement precision is shown in Fig. 10(c) with absolute values of raw velocity fields ($\sqrt{u^2 + v^2}$), and it is calculated by 50 PIV snapshots. It can be seen that the maximal RMS in Fig. 10(c) are less than 1 m/s (the free-stream in PIV experiments is 10 m/s). The present instantaneous PIV snapshots merely are used to qualitatively visualize vortex structures, not quantitatively, so the precision is sufficient.

The instantaneous PIV snapshots in Fig. 10 present the variation in positions of asymmetric vortices. The vortex pattern is a typical three-vortex structure in which the two vortices near the wall are very apparent, and the highest vortex marked by a white dashed circle can be out of field views at any instant due to unsteady heaving as shown in Fig. 11(c)–(e). Although the highest vortex has larger magnitude of heaving, it is far from the body wall, contributing less to fluctuations of pressures and side forces. The wall fluctuations are chiefly attributed to two lower vortices which change their positions with time, but

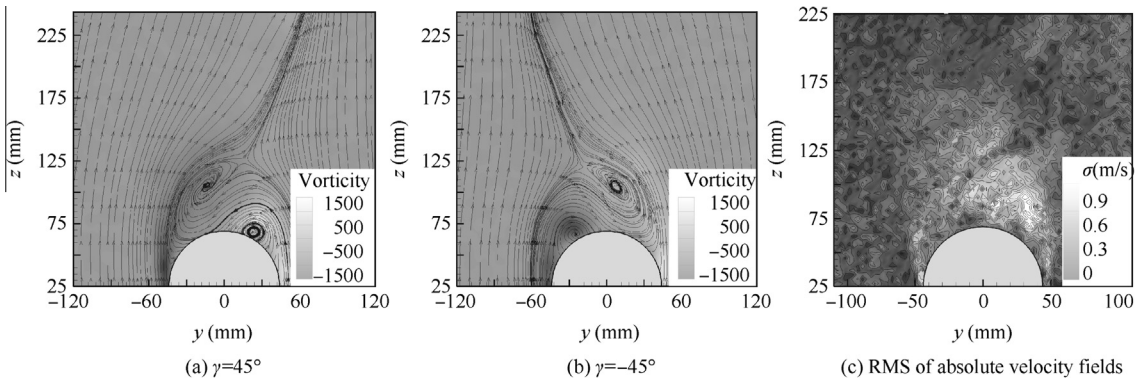

Fig. 10 Averaged results with 50 snapshots of PIV at $\alpha = 70°$ and $x/D = 2.5$.

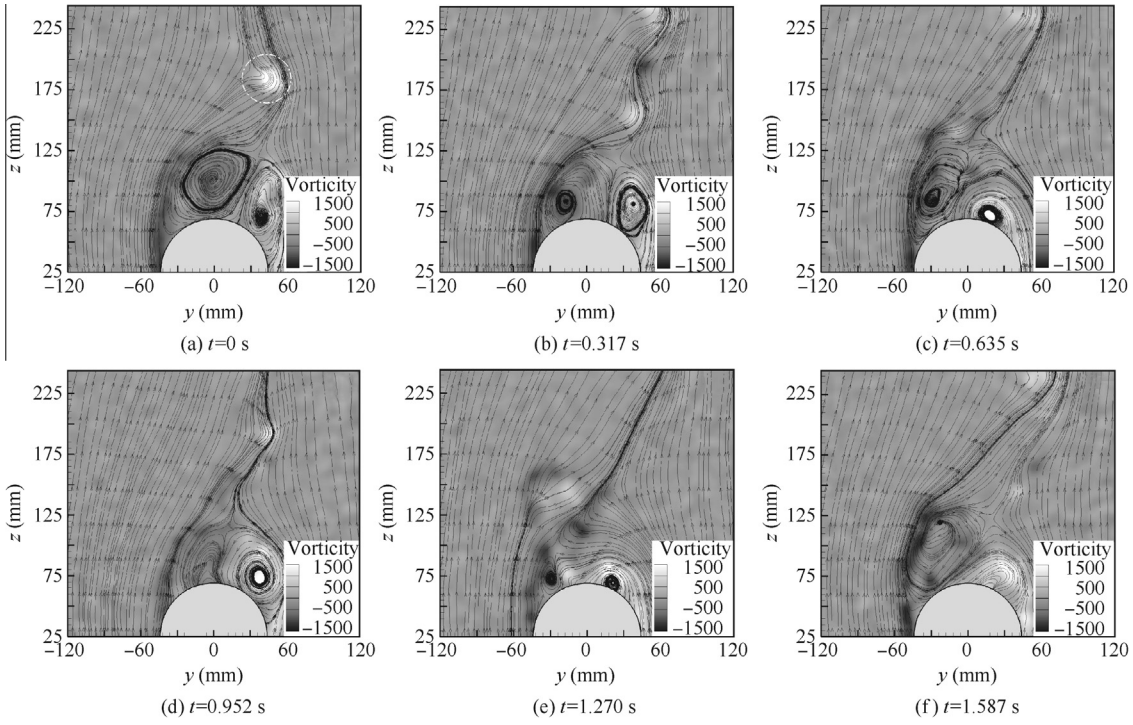

Fig. 11 Instantaneous PIV results with $\gamma = 45°$ at AOA = 70°, $x/D = 2.5$, from rear view (PIV snapshots at a sampling rate of 3.15 Hz).

not shedding. The time-averaged vortex structure is still dominated by tip perturbations, as indicated in Fig. 10(a) and (b), and this role of tip perturbation can also be found from the instantaneous flow structures in Fig. 11. The highest vortex is always located on the right side with $\gamma = 45°$.

4. Discussions

The results above indicate that low-frequency oscillations exist for asymmetric vortex flows over the forebody part of a slender body at 65–80° AOAs. The vortex oscillation induces large amplitude fluctuations in pressures and side forces which are strong enough to be able to influence yawing stability of aircraft. The fluctuation frequencies are much lower than the frequency of Karman vortex shedding. The pressure distributions and vortex patterns indicate that the vortices oscillate around time-averaged asymmetric vortices.

The results above also show that the separation types of boundary layers have an important effect on the low frequency fluctuation, and the fluctuation can be reduced significantly at critical Reynolds numbers, as indicated in Figs. 5 and 9. The Reynolds numbers in our experiments just cover a subcritical regime and an earlier phase of a critical regime, completely not attaining a postcritical regime. In terms of previous research,[22,23] the asymmetry level of vortices over a slender body is the highest at a subcritical and postcritical regime, inducing very large side forces, but at a critical regime, the asymmetric vortex system will lose regular structures due to boundary layer transition, the generated side forces gradually approach to zero with increasing Reynolds numbers. Therefore, although the low frequency fluctuations are weakened when Reynolds number is increased into a critical regime, it is much likely to recover at a postcritical regime. However, the conjecture needs to be further verified

experimentally in wind tunnels capable to provide higher Reynolds numbers.

In addition, it should be noted that the flow mechanism causing the asymmetric vortex oscillations are not clear. A few possible mechanisms can be proposed, but need to be proved further. One possibility responsible for the vortex oscillation is flow absolute instability, in other words, the oscillation is an intrinsic nature of the flow. This conjecture can be verified or excluded using stability analysis. Another possibility is that vortex breakdown induces the vortex oscillation. Since the AOAs are sufficiently high, the asymmetric vortices should have breakdown at least downstream. Previous research has revealed that vortex breakdown are highly unsteady, and the breakdown points can move back and forth. Therefore, the unsteadiness of vortex breakdown can also induce vortex oscillations. However, the present investigation cannot study the breakdown phenomenon of asymmetric vortices due to a limitation of experimental methods. Probably, the PIV snapshot along a vortex core axis can be used to identify the vortex breakdown, but since the asymmetric vortex core is not a straight line, this type of PIV measurement is very difficult to be performed.

5. Conclusions

The unsteady characteristics of asymmetric vortex flows over an ogive-cylinder body were investigated experimentally in a range of Reynolds numbers of 0.6×10^5–2.5×10^5, and some conclusions can be drawn as follows.

A new type of unsteadiness with low frequencies and large amplitudes was found for the asymmetric vortex flow around the fore-body of a slender body at angles of attack of 60–80°. The vortex unsteadiness produces a large fluctuation of side forces, and the peak-to-peak amplitudes of the sectional side force coefficients can reach 2.0. The large-amplitude fluctuation exists in a range of subcritical Reynolds numbers of 0.6×10^5–1.8×10^5, and when the Reynolds numbers rise up to a critical regime, the fluctuation amplitudes are reduced greatly. Within the present Reynolds numbers and angles of attack, the reduced frequencies are between 0.038 and 0.072, much less than the frequency of Karman vortex shedding of 0.21. The reduced frequencies decease with increasing Reynolds numbers, but rise up with increasing angles of attack.

The fluctuation of side forces comes from periodic oscillations of asymmetric vortex wakes. Since the time-averaged vortex patterns are asymmetric, whose orientations are dependent on azimuthal locations of a tip perturbation, the vortex oscillation is a type of unsteady oscillation around a time-averaged asymmetric vortex structure. The periodic vortex motion leads to pressure fluctuations on the leeward side of a fore-body, and the pressure signals on the left and right of a leeward side have the same frequency, but a phase difference of 180°.

Acknowledgement

The project was supported by the National Natural Science Foundation of China (No. 11272033).

References

1. Thomson KD, Morrison DF. The spacing, position and strength of vortices in the wake of slender cylindrical bodies at large incidence. *J Fluid Mech* 1971;**50**(4):751–83.
2. Lamont PJ, Hunt BL. Pressure and force distribution on a sharp-nosed circular cylinder at large angles of inclination to a uniform subsonic stream. *J Fluid Mech* 1976;**76**(3):519–59.
3. Bridges DH, Hornung HG. Elliptic tip effects on the vortex wake of an axisymmetric body at incidence. *AIAA J* 1994;**32**(7):1437–45.
4. Levy Y, Hesselink L, Degani D. Systematic study of the disturbances and flow asymmetries. *AIAA J* 1996;**34**(4):772–7.
5. Chen XR, Deng XY, Wang YK, Liu PQ, Gu ZF. Influence of nose perturbations on behaviors of asymmetric vortices over slender body. *Acta Mech Sin* 2002;**18**(6):581–93.
6. Deng XY, Wang G, Chen XR, Wang YK, Liu PQ, Xi ZX. A physical model of asymmetric vortices flow structure in regular state over slender body at high angle of attack. *Sci China Ser E* 2003;**46**(6):561–73.
7. Yang YJ, Cui EJ, Zhou WJ. Numerical study about asymmetric vortex flow around a slender body at high incidence. *Acta Mech Sin* 2004;**36**(1):1–8 Chinese.
8. Ming X, Gu YS. Control of asymmetric flow fields of slender bodies at high angle of attack. *Chin J Aeronaut* 2006;**19**(2):168–74.
9. Tian B, Li HX, Meng XS, Luo SJ, Liu F. Flow control of conical fore-body with single-pulsed discharge plasma. *Acta Aerodyn Sin* 2012;**30**(5):680–4 Chinese.
10. Williams D. A review of fore-body vortex control scenarios. 1997. Report No.: AIAA-1997-1967.
11. Snarski SR. Flow over yawed circular cylinders: wall pressure spectra and flow regimes. *Phys Fluids* 2003;**16**(2):344–59.
12. Lam K, Lin YF, Zou L, Liu Y. Investigation of turbulent flow past a yawed wavy cylinder. *J Fluids Struct* 2010;**26**(7):1078–97.
13. Yeo DH, Jones NP. Characterization of flow oblique to a circular cylinder with low aspect ratio using 3-D detached eddy simulation. *J Wind Eng Ind Aerodyn* 2011;**99**(11):1117–25.
14. Zeiger MD, Telionis DP, Vlachos PP. Unsteady separated flows over three-dimensional slender bodies. *Prog Aerosp Sci* 2004;**40**(4):291–320.
15. Degani D, Schiff LB. Numerical simulation of the effect of spatial disturbances on vortex asymmetry. 1989 Jan. Report No.: AIAA-1989-0340.
16. Degani D, Zilliac GG. Experimental study of nonsteady asymmetric flow around an ogive-cylinder at incidence. *AIAA J* 1990;**28**(4):642–9.
17. Degani D. Effect of splitter plate on unsteady flows around a body of revolution at incidence. *Phys Fluids A Fluid Dyn* 1991;**3**(9):2122–31.
18. Zilliac GG, Degani D, Tobak M. Asymmetric vortices on a slender body of revolution. *AIAA J* 1991;**29**(5):667–75.
19. Hoang NT, Rediniotis OK, Telionis DP. The dynamic character of the hemisphere-cylinder wake. *Exp Fluids* 1999;**26**(5):415–22.
20. Ma Y, Liu PQ, Deng XY, Shao YF. The characteristics of nose vortices and Karman vortices in the flow over slender body at high angles of attack. *Exp Meas Fluid Mech* 2004;**18**(2):65–70 Chinese.
21. Ma Y, Liu PQ, Deng XY, Shi JL. The unsteadiness study of nose vortices in the flow over slender body at high angles of attack. *Exp Meas Fluid Mech* 2004;**18**(4):72–7 Chinese.
22. Ma BF, Deng XY, Chen Y. Effects of forced asymmetric transition on vortex asymmetry around slender bodies. *AIAA J* 2007;**45**(11):2671–6.
23. Lamont PJ. Pressures around an inclined ogive cylinder with laminar, transitional, or turbulent separation. *AIAA J* 1982;**20**(11):1492–9.

Ma Baofeng is an associate professor in the Institute of Fluid Mechanics at Beihang University. He mainly focuses on the investigation of unsteady flows and separated vortex flows using experimental and computational methods.